

Surface texturing of aluminium alloy AA2024-T3 by picosecond laser: Effect on wettability and corrosion properties.

J.I. Ahuir-Torres^a, M.A. Arenas^a, W. Perrie^b, G. Dearden^b and J. de Damborenea^{a*}

^a Department of Surface Engineering, Corrosion and Durability, Centro Nacional de Investigaciones Metalúrgicas, CENIM-CSIC. Av. Gregorio del Amo 8, 28040 Madrid, Spain.

^b Laser Engineering Group, School of Engineering, University of Liverpool, Brownlow Hill, Liverpool L69 3GQ, United Kingdom.

* Corresponding Author: jdambo@cenim.csic.es

Abstract

The effects of laser texturing on the corrosion and wettability of AA2024-T3 using an IR Nd:Vanadate picosecond (ps) laser was studied. Three types of texture patterns were generated: dimples with 5 % and 50 % area density (percentage of surface area textured); cross groove patterns with an area density of 64 %; and concentric ring patterns with an area density of 70 %. For the higher area densities, the surface character changed from hydrophilic to hydrophobic. The evolution of the open circuit potential over time, potentiodynamic polarization curves and electrochemical impedance spectroscopy were then investigated and analysed. The results revealed that ps laser surface texturing did not modify the corrosion behaviour of AA 2024-T3 in the test solution.

KEYWORDS:

Aluminum alloy; laser texturing; SEM; wettability; corrosion

1. Introduction

Since the invention of the first laser by Theodore Maiman in 1960, laser technology and its applications in the field of materials processing have been well established. Much of this is due to the special attributes of laser beams: monochromaticity, spatial and temporal coherence, directionality and hence the ability to create ultra-high intensities at a focus. Such features make it possible, for example, to provide a large flow of energy precisely to a specific spot on a material surface and enable the development of a large variety of surface treatments based on heating, melting and vaporization [1]. Taking advantage of the development of pulsed lasers, short (μs - ns duration) pulses allow thermal effects of laser radiation to be limited almost exclusively to the treated areas, while ultra-short (ps - fs duration) pulses can eliminate thermal effects almost completely. This last feature opens up new possibilities for treating materials, including the texturing of surfaces by laser ablation. Using this technique, the topography of a material may be modified to give enhanced surface properties (and added functionality), but without affecting its structural properties [2,3].

Among various alloys of technological interest, aluminium alloys (especially AA2024) are highlighted due to their exceptional strength-to-weight ratio [4]. By modifying the topography of the material, it may be possible to achieve additional advantages to those already offered by the alloy, such as: the generation of compressive stresses that could avoid stress corrosion cracking; or increasing adhesion capacity for use with structural adhesives; or improved tribological properties by creating micrometric reservoirs for lubricants. The fact remains, however, that many laser treatments produce a thermal effect on the material which, when treating a significant proportion of surface area, can change its resistance to corrosion. Whether the change is a negative or positive one can depend on the specific alloy and treatment conditions applied. Liu et al. [5] investigated the corrosion performance of three aluminum alloys, including AA 2024-T3, after laser bending with a 250 W continuous wave CO_2 laser. The laser treatment induced different degrees of sensitization in each alloy, leading

to severe inter-granular corrosion attack for both AA 2024-T3 and AA 7075-T6 cases.

However, in the case of AA 5083-O, the resistance to inter-granular corrosion was improved, while for AA 7075-T6 post-forming heat treatment led to full recovery of its properties without any change in dimensions. Viejo and co-workers [6] found that laser surface melting of AA 2050-T8 with an 80 W excimer laser (wavelength 248 nm; pulse length 13 ns) led to enhanced corrosion resistance, attributed to the relatively uniform 20 μm depth melted layer largely free of constituent particles. In the same vein, Xu et al [7] used a Nd:YAG laser for surface melting of an AA 6013 producing a melted layer of a few hundred micrometres with fine dendritic structure and removing the coarse second phase particles. As a result of it, laser treated samples showed a reduction in corrosion current density at least one order lower in magnitude than that of the untreated specimens.

Laser shock peening also has been used for improving pitting potential of aluminium alloys, which ensures higher corrosion resistance [8]. However, laser shock peening processes require multi-Joule, ns ‘giant-pulse’ lasers (e.g. Q-switched Nd:YAG or Nd:Glass), with a large footprint and only ~ 10 Hz pulse repetition rate – considered to be a specialist technology and not generally available as affordable and easy-to-use commercial lasers.

It is clear from the above that, in general, laser surface engineering has been widely used to modify different alloys resulting in greater corrosion properties due to the formation of novel microstructures [9].

However, it is no less certain that laser processes with a more thermal effect could tend to produce negative effects on corrosion properties. In contrast, the texturing of metallic material surfaces by ablation with ultra-short pulse lasers may be a viable way of avoiding such thermal effects. For example, Toloei and co-workers, addressing relevant ablation studies, found that the corrosion properties of nickel could be improved by ablation texturing with a 30 ns pulse length Cu:Br laser [10]. In this regard, ps pulse length lasers are now gaining

increasing interest. Currently, ps lasers have been scaled to high average powers > 200 W with MHz pulse repetition rates. Hence, optical beam engineering techniques for ultra-short pulse lasers have been developed to enable maximum usage of available laser energy. Here, viable approaches include high speed laser beam scanning with polygon mirrors for MHz systems and multi-beam parallel processing and periodic structuring with ‘fixed-recipe’ optics (e.g. diffractive optical elements, DOE) or dynamically variable spatial light modulation [11]. Collectively, these technologies have the potential to deliver orders of magnitude increases in process throughput for surface patterning and structuring applications. Compared to fs laser technology, ps lasers are seen as potentially providing higher average powers for industrially relevant process rates, but at lower cost with reduced system complexity and improved reliability.

As far as the authors are aware, there has been no previous study into the effect of ps laser texturing on the corrosion resistance of AA 2024-T3. Hence, the aim of this work has been to study whether the creation of different patterns (dimples, crossed grooves and concentric rings) of surface texture on AA 2024-T3, using ps laser ablation, can have negative effects on the alloy’s corrosion behaviour, as tested in diluted NaCl solutions.

2. Experimental

Commercial AA2024-T3 aluminium was supplied by ALUSTOCK. The alloy had the following composition (wt %):

Cu 4.30; Mg1.27; Mn 0.62; Fe 0.30; Si 0.16; Ti 0.043, Zn 0.039; Cr 0.018; Al (balance)

Specimen dimensions were 15x15 mm, with an average thickness of 1.8 mm. Prior to laser texturing, the alloy was mirror-finished using a wet grinding on SiC papers down to 1200 grit and final polishing with colloidal silica suspension (0.04 µm). The initial roughness of the specimens was of 0.015 ± 0.001 µm.

Figure 1(up) shows an optical micrograph of a mechanically polished and etched (Keller's reagent, 10 seconds) cross-section of AA2024-T3 aluminium alloy before laser treatment. The micrograph shows even distribution of the different intermetallics presented in the alloy. As it has been highlighted in the literature by different authors, the microstructure of AA2024-T3 is very complex, comprising an aluminium matrix and a wide range of intermetallics [12].

Hughes et al. [13] analysed by Electron probe microanalysis (EPMA) a range of phases in AA2024-T3. It was found up to 18000 intermetallic particles with nine different compositions around S-phase/ θ -phase composites as well as particles containing Al, Cu, Fe, Mn and Si, giving an idea of the complexity of the system under study. It is also accepted that the large majority of intermetallics is S-phase (Al_2CuMg), approximately 60 % of intermetallic particles [14]. Another group of intermetallic particles are Al-Cu-Mn-Fe-Si-containing, with a range of compositions including Al_7CuFe_2 , Al_6MnFe_2 , $(\text{Al,Cu})_6\text{Mn}$, and a number of undetermined compositions in the class $\text{Al}_6(\text{Cu,Fe,Mn})$. For the purposes of this paper, only a characterization of the main intermetallics has been done. **A detail of the microstructure obtained by scanning electron micrograph is observed in Figure 1(down).** According to the EDS analysis the main constituents found were S-phase (Al_2CuMg), mainly precipitated at grain boundaries, θ -phase (Al_2Cu) and different AlCuFeMn(Si) intermetallics.

The laser used to create the various textures was a solid state Nd:Vanadate (Nd:YVO_4) laser (High-Q model IC381), with a pulse duration of 10 ps and IR output wavelength of 1064 nm. The beam had high temporal and spatial stability in a TEM_{00} mode ($M^2 \leq 1.32$). The laser was controlled by laser specific (HQL GUI) software. Sample surfaces were positioned on a precision X-Y-Z motion table (Aerotech A3200, run under NView MMI software) at the focal plane of a 100 mm focal length f-theta lens within a beam scanning galvo (Nutfield XLR8-10). Observation of plasma emission near the ablation threshold provided a method to determine the optimum sample surface Z-height, with sufficient sensitivity to position within $\pm 50 \mu\text{m}$ of the optimum focal plane. Consequently, the sample surface always remained

within the depth of focus for processing, $\Delta Z = \pm 50 \mu\text{m}$ (\ll Rayleigh length $Z_r \sim \pm 0.6 \text{ mm}$).

Once a sample surface was brought to the focal plane, scan patterns were created in a (SCAPS GmbH) galvo mirror control software interface. A schematic diagram of the experimental laser beam delivery setup is presented in Figure 2.

Two methods were used to generate a variety of textures on the alloy surface in an ambient air environment: i/ applying a known number of laser pulses of specific energy to a single site or ‘spot’ (while at zero motion), then moving the sample to repeat this in sequence at many uniformly spaced sites, to create arrays of dimples (Figure 3 a) ; ii/ scanning at known velocities, synchronized with the pulse repetition frequency of the laser, thus ablating material using a continuous train of partially overlapping laser pulses of known energy, to make continuous surface features, (Figure 3 b). It was anticipated that careful selection of pulse frequency and overlap would enable uniform or smoothly-varying features such as crossed grooves and concentric rings (Figure 3 c and d). Density percentage was calculated by numerical method. Depending on the desired textures, different expressions were used. For the case of arrays of dimples:

$$r_c = \left(\frac{\pi \times D^2}{4 \times l^2} \right) \times 100 \quad (1)$$

where r_c is the density percentage of dimples, D is the dimple diameter and l the distance between centres of the dimples.

For the crossed grooves:

$$r_{sc} = \left(1 - \frac{(D_M - A) \times (D_m - A)}{D_M \times D_m} \right) \times 100 \quad (2)$$

where r_{sc} is the density percentage of crossed grooves; D_M and D_m are the major and minor diagonal respectively and A the width of the groove.

Finally, for the concentric rings:

$$r_{AC} = \frac{2 \times (\pi \times \frac{D^2}{4} + \pi \sum_1^N ((R_i')^2 - (R_i)^2))}{l^2} \times 100 \quad (3)$$

where r_{AC} is the density of concentric rings; R_i' and R_i are the external and inner radius respectively of the ring; D is the diameter of the central dimple and l the distance between centres of each concentric rings.

Over the full set of experiments, laser pulse energies of the order 6-7 μJ , scanning velocities of ~ 2.4 mm/s and pulse repetition frequencies in the range 5-10 kHz were used. The pulse length was fixed at 10 ps for this laser system, while the ratios of pulse energy to focused beam spot size gave fluencies in the range 0.1-1 J/cm^2 . Our research experience of machining pure Al with a 10 ps laser [15] was considered in broadly selecting process parameters to arrive at this range of fluencies, so as to operate marginally above the ablation threshold of the material. This approach was preferred in seeking uniform texture features, by achieving consistent absorption of laser energy, pulse-to-pulse. In contrast, fluencies much higher than the ablation threshold can result in excessive ablation depth per pulse (leading to heat diffusion and melting), or unwanted damage mechanisms. The alloy surface after polishing would have localized micro-scale variations in topology (asperities) as well as sub-surface grain structure and inclusions. Therefore, in operating close to the ablation threshold, it was considered that a uniformly shaped dimple could not be readily created with a single laser pulse. Instead, our previous studies on ps laser ablation of base metals had shown that irradiation with multiple, close-to-threshold pulses allowed a uniform crater or dimple to successfully develop.

The morphology and geometry of the textured surfaces were studied using an Olympus GX 51 optical microscope, while the topography of the textures was evaluated using an interferometric confocal Sensofar PL μ 2300 profilometer.

Contact angle (θ) measurements were carried out in a relative humidity and temperature maintained at 40 % and 293 K (22 °C), respectively using a Theta (Attension) optical tensiometer with automatic distilled water dispenser. Sessile drops (3 μ L water) were recorded in normal mode with a trigger within 18 s from the moment the drop touched the surface. Each measurement for individual surface texturing was done in triplicate with variability within ± 5 %.

Electrochemical tests were performed in 0.06 M NaCl solution at room temperature, using a Gamry Reference 600 potentiostat. The electrochemical cell used was a three- electrode cell; where an Ag / AgCl (3 M KCl) electrode was the reference electrode, the counter-electrode was a platinum wire, and the working electrode, was the sample under study. The exposed area of the samples was 0.13 cm². The volume of electrolyte used for electrochemical tests was 30 ml. All the tests were done in aerated conditions.

Before the polarization curves, the evolution of the open circuit potential (OCP) was recorded in the test solution for an immersion period of 2 hours, after which the potentiodynamic curves were made. A potential step of -0.3 V with respect to the corrosion potential was applied, starting the sweep in an anodic direction at a rate of polarization of 0.16 mV/s until reaching a potential 0.1 V vs. Ag/AgCl (3 M KCl); or a limit value of 0.25 mA/cm². The reverse sweep was then started until reaching the initial potential.

The electrochemical impedance spectroscopy measurements were performed at different immersion times in other batch of samples, from 2 to 96 hours, with the aim of studying system evolution with regard to the test duration. A frequency range of 100 kHz to 10 mHz was used, recording 10 points per decade. The amplitude of the sinusoidal signal was 3.5 mV. The impedance tests were carried out potentiostatically vs. the corrosion potential.

Simulations were performed using Zview software.

All electrochemical tests were conducted at least in triplicate.

Finally, SEM analysis was made by field emission gun scanning electron microscopy (FEG-SEM) utilizing a Hitachi S 4800 J instrument equipped with energy dispersive X-ray -EDX-detector.

3. Results and Discussion

3.1. Laser texturing and topographic characterization

Using approaches described above, the following textures were successfully produced: dimple patterns with textured area densities of 5 % and 50 %; crossed groove patterns of area density 64 % (with crossing angle 45°); concentric ring patterns of area density 70 %. The latter pattern was made up of the repetition on the surface of a texture composed of a central dimple surrounded by four concentric rings.

Table I shows the conditions of pulse energy, pulse number and scan speed used in generating the evaluated textures.

Applying fluencies a few times above the ablation threshold resulted in efficient material evaporation, while minimizing any melt layer, thus leading to precision micro-machining. Based on data for pure aluminium, the estimated lattice heating time (~ 2 ps) was shorter than the pulse length (10 ps) and so a consideration of heat diffusion is justified through the following analysis. The optical penetration depth in pure Al (l_{opt}) is ~ 7 nm [16], while the thermal penetration depth $l_{th} \sim \sqrt{2D_{liq}\tau_p}$ is ~ 25 nm, where D_{liq} is the thermal diffusivity of liquid Al ($0.32 \text{ cm}^2\text{s}^{-1}$) and τ_p is the pulse length (10 ps). Al melts rapidly after exposure, due to its low melting point 933 K (660 °C) and ultrafast lattice heating time (electron-phonon coupling time) of ~ 2 ps $\ll \tau_p$ [15]. To bring a layer with thickness $l_{opt} + l_{th} \sim 32$ nm to its boiling point 2743 K (2470 °C) would require a threshold fluence of $F_{th} \sim 0.2 \text{ Jcm}^{-2}$, while evaporating this layer would require a fluence of $F \sim 1.0 \text{ Jcm}^{-2}$. This limited heat diffusion

and almost instantaneous electron-lattice heating ensure that a thin surface layer is thus brought rapidly to the boiling point, ~ 2773 K (2500 °C) during ps laser ablation.

In Figure 4, the optical micrographs of the laser-treated surfaces are presented. In the micrograph of Figure 4a, for dimples with a density of treated area equal to 5 %, traces are distinguishable near the dimples because the pulse rate exceeds a level that would match the translation speed. This makes it possible to produce intermediate impacts that, in any event, do not appear to have significant effect on the surface. When the dimple density per unit area is increased, Figure 4b, the traces disappear. In the case of crossed grooves with an area density of 64 %, Figure 4c, and concentric rings at 70 %, Figure 4d, it can be observed that the generated surface patterns are very regular.

The topographic images and profiles of the different texture patterns are shown in Figure 5. The patterns, as can be seen in all images, are regular both in their distance between textures and their geometry. Each dimple has a diameter of 37 ± 2 μm and a depth of 4.0 ± 0.4 μm . In the case of grooves, the width is 43.0 ± 2.0 μm and the depth is 4.5 ± 0.4 μm . Finally, the concentric rings (made up of a central dimple plus four circular surrounding grooves) show the same dimensions as the above patterns for dimples and grooves. It therefore appears that varying the direction of laser scanning does not affect the width or the depth of texture.

The existence of intermetallics is observed in the generated texture background, as shown in the SEM images for the crossed grooves and concentric rings (representative for all textures), Figure 6. The EDS analysis (not shown here) of these particles revealed the presence of coarse Al-Cu-Fe-Mn-(Si), θ -phase and S-phase intermetallics that were originally present in the material surface and became more exposed after ablation of the treated area. The combination of laser fluence and (ultra-short) laser-material interaction time produces ablation of the aluminium matrix surface but it does not have enough interaction time to produce redissolution of the intermetallics. **Two nanostructures are also observed in grooves**

and concentric rings, Figure 6. In the grooves, periodic structures, known as Laser Induced Periodic Surface Structure (LIPSS) have developed due to multi-pulse exposure, while in the concentric rings, LIPSS are only observed on the edges of the tracks, whereas a random nanostructure is formed in the centre of the track.

3.2 Wettability and Corrosion behaviour

Figure 7 shows the variation of the contact angle with the four textured generated in the AA2024-T3 alloy (as received, 5 % dimples, 50 % dimples, 64 % crossed grooves and 70 % concentric rings). As can be seen, the un-textured samples and the surface with 5 - 50 % dimples showed contact angles of 65° and 75° respectively, therefore being hydrophilic. However, the crossed grooves and the concentric rings had a value close to 100° changing its character to hydrophobic. It is generally accepted that the change in the wettability properties of the materials depending upon the microstructure. Kam el al [17] treated AISI 316L stainless steel with a femtosecond laser allowing the development of micro-cone textures on the surface by effect of laser pulses at high repetition. In this way it was possible to obtain both hydrophilic and hydrophobic surfaces on stainless steel, simply by changing the fluence conditions.

As it has already been highlighted in Figure 4, the laser treatment changed the smooth initial surface due to the ablation of the alloy, varying the surface topography more or less in accordance with the laser parameters as well as the type of texture. Figure 8 pictures the changes in roughness induced changes by the laser treatment. As it can be seen, the roughness reached values substantially greater for high density textured surfaces when compared to un-textured or samples with less textured area. Although different factors affect the wettability, surface chemistry for instance, the roughness seems to play a fundamental role in the change of the wetting behaviour. It has been established in the literature that microtextured surfaces can change its hydrophobicity mainly by two different mechanisms: Wenzel and Cassie-

Baxter [18]. Though differing to explain how it takes place, at certain degree of roughness both mechanisms can coexist on the same surface [19]. Regardless of the specific mechanism, the hydrophobicity is reached by the formation of regular protuberances or pillars on the surface that prevent liquids to wetting the surface. If these protuberances (in the shape on nanopillars or nanocones) define a hierarchical surface structure, superhydrophobicity can be achieved. In our case, the morphology of the pattern and the texturing conditions selected to generate it, did not allow to form cones or piles but the ablated structure is enough to change from hydrophilic to hydrophobic. Similar results have been obtained by Kietzig and co-workers [20] on different iron based alloys and titanium alloy. In the same line, Ta et al [21] have demonstrated that laser texturing can be used as a simple method for changing the wettability of the metallic alloys.

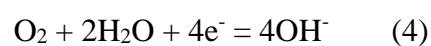
In principle, it could be expected than surface exhibiting the lower contact angle should present the highest corrosion resistance. However, it is not a direct cause-effect relation in particular when the surfaces present just a hydrophobic behaviour.

Figure 9 shows the evolution of the open circuit potential with respect to the immersion time of the reference alloy and all texturized samples in an NaCl 0.06 M solution. It can be observed that the potential shows a similar trend both in the polished samples as well as in the various texture patterns. The potential fluctuates for all tested conditions around -0.55 ± 0.03 V vs. Ag/AgCl (3 M KCl) throughout the immersion period evaluated. Although this parameter only provides information on the thermodynamic stability of the system, its fluctuation indicates the activity of the system, due to the competitive process between the generation and growth of pitting and passivation of the material. This phenomenon is caused by the presence of AlCuFeMn intermetallics as well as θ -Al₂Cu and S-Al₂CuMg phases that present a different electrochemical behavior with respect to the Al solid solution matrix [22]. The Al₂Cu particles have a cathodic nature in comparison to the surrounding Al matrix, causing a localized corrosion process around them which then promotes their fall-off from the

surface. In contrast, the Al₂CuMg intermetallics show an anodic behavior, dissolving preferentially with respect to the matrix in the NaCl solution [23]. The Al matrix spontaneously tends to be passive. The interaction between the different processes that are taking place on the surface is what ultimately produces the fluctuations that are gathered in the corrosion potential. Therefore, this would appear to indicate that no large differences in corrosion are expected.

The polarization curves of the tested samples are compared in Figure 10. All samples exhibited similar features regardless of whether they are texturized. At potentials higher than corrosion potential (E_{corr}), the anodic branch showed an activation control (charge transfer controlled anodic metal dissolution). The anodic branch is practically horizontal, indicating that the alloy is very active in this medium, and that the pitting potential coincides with the corrosion potential. As it was explained before this active behaviour is due to the existence of intermetallics of a different electrochemical nature. Hughes et al. [13, 24] identified that the corrosion process begins with the localized attack of S phase which causes its selective dissolution. The process then continues with the selective attack of the aluminium matrix around the cathodic AlCuFeMn particles, and finally around the (Al, Cu) intermetallics.

For cathodic potentials lower than E_{corr} , the system presented a diffusion control due to oxygen reduction. The cathodic branch, ranging from -0.88 to -0.50 V vs. Ag/AgCl (3 M KCl), shows an infinite slope, indicating that in all cases the system is controlled by diffusion (cathodic control) and is characterized by an increased potential that does not induce changes in the intensity response. That is, it is not possible to capture more electrons on the surface per unit time in the cathodic semi-reaction, which in this medium is the oxygen reduction:



According to Cheng et al [25] the OH^- reacts with the Al ions to form aluminium hydroxide ($\text{Al}(\text{OH})_3$) on the electrode and it could therefore block the oxygen reduction sites on the electrode surface.

When this concentration polarization phenomenon occurs, the corrosion current density is determined by limiting diffusion current density of oxygen reduction, i_d , which represents the maximum rate at which the oxygen reduction process on the electrode surface occurs, and it corresponds to the value of the current density in the vertical portion of the cathodic branch.

Table II provides the values of the main electrochemical parameters deduced from the polarization curves. As it can be appreciated all samples showed similar E_{corr} , i_d and i_{corr} (calculated from anodic Tafel slope). Only the crossed groove pattern at 64 % describes an i_d one order of magnitude higher, $20 \mu\text{A}/\text{cm}^2$ than the other samples, $\sim 4 \mu\text{A}/\text{cm}^2$.

It is important to emphasize that the polarization curves provide useful information on kinetics rather than corrosion mechanisms itself. It is not surprising therefore that the curves revealed an activation control on the anodic reaction together with a concentration limited cathodic behaviour (diffusion). So, the determination of the corrosion current density, i_{corr} , in these kind of systems can be done by the extrapolation of the anodic Tafel slope with the limiting diffusion current density (i_d) for oxygen reduction back to E_{corr} [25]. Further information about the corrosion mechanism of the textured samples can be attained through the electrochemical impedance spectroscopy.

As can be seen in Figure 11, there is a widespread process of corrosion after the polarization curve. Coarse Al-Cu-Fe-Mn-(Si) particles and θ -phase are cathodic sites, producing anodic corrosion of the adjacent aluminium matrix. On the other hand, S-phase (Al_2CuMg) presented at grain boundaries, are anodic with respect to the adjacent grain matrix, leading to a preferential dissolution of S- phase. In fact, according to literature [26] the copper of this S-phase is dissolved and deposited around the particle while the rest is dissolving.

In Figure 12, the Bode diagrams are shown for the electrochemical impedance spectra corresponding to the un-textured and textured aluminium alloy 2024-T3 samples (diagrams for 5 % dimples are not shown). Figure 13 pictured a comparison of all samples after 48 hours of immersion.

In all cases, the impedance diagrams show two time constants, from the beginning of immersion at 2 hours, until the end of the test at 96 hours. These time constants appear in the same frequency ranges in the Bode diagrams; the first one at medium frequencies with a maximum phase angle of 70° in the Bode plots, and a second one at low frequency. This second time constant is viewed as a diffusion tail in the Nyquist diagram.

The values of the electrochemical parameters obtained from the experimental data for the various samples and immersion times are shown in Table III. As can be seen in the table, all samples have similar values regardless of the test time.

From the impedance module Bode diagrams it is possible to obtain the resistance of the electrolyte, in the high frequencies range, R_1 , whose value is practically constant at $\sim 25 \Omega \cdot \text{cm}^2$.

The time constant described in the medium frequencies shows a slope in the module Bode diagrams (1st slope) of -0.8, as well as a capacitance (1st capacitance) of $\sim 70 \mu\text{F}/\text{cm}^2$ and a resistance (R_2) with values on the order of $2000 \text{ k}\Omega \cdot \text{cm}^2$.

The second time constant, which is placed in the low frequency range, exhibits a second slope in the module Bode diagrams of approximately 0.4.

To model this behaviour, the equivalent circuit shown in Table IV was proposed. This circuit comprised the electrolyte resistance, R_e , in series with a constant phase element, CPE_{dl} , representing the double layer formed at the metal-electrolyte interface, which is in parallel with resistance, R_{ct} , the charge transfer resistance, and which in turn is in series with a

constant phase element, CPE_{dif} , representing the diffusive process observed at low frequency. This circuit has been traditional in corrosion studies of aluminium alloys and still applies today to simulate the electrochemical response of aluminium 2024-T3 in NaCl [27].

The simulated data using the equivalent circuit described above is shown in Table IV. The χ^2 values for the simulations were of the order 10^{-4} and confirm the validity of the fitting applied.

The electrolyte resistance, R_e , is similar in all samples and is about $\sim 30 \Omega \cdot \text{cm}^2$.

The n_{dl} exponent of CPE_{dl} presents values of 0.9 that indicate that this constant phase element is associated with a capacitor. Furthermore, the CPE_{dl} values increase with immersion time.

This value varies from 70 to $100 \mu\text{Ss}^n/\text{cm}^2$ for the textured surfaces, while the polished surfaces range from $90 \mu\text{Ss}^n/\text{cm}^2$ at 2 hours of immersion to $200 \mu\text{Ss}^n/\text{cm}^2$ at 96 hours of immersion. The R_{ct} obtained by simulation had values between 1-3 $\text{k}\Omega \cdot \text{cm}^2$.

CPE_{dif} and n_{dif} values are similar in all samples. The CPE_{dif} is on the order of mSs^n/cm^2 indicating a diffusive behaviour even though n_{dif} values are approximately 0.75 which is slightly high for being an infinite length Warburg impedance.

In Figure 14, the experimental and simulated spectra are compared for all the samples after 72 hours of immersion. These Figures show that there is good agreement between experimental and simulated data. It is barely possible to distinguish that the spectra are slightly different in the low frequency range due to the high dispersion of experimental data.

As described above, the time constant revealed at low frequencies is related to diffusive process. The relationship between Warburg impedance, Z_ω , and the diffusion coefficient, σ , is [28]:

$$Z_\omega = \left(\frac{2}{\omega}\right)^{\frac{1}{2}} \sigma \quad (5)$$

From (5) the value of the diffusion coefficient can be easily determined according to:

$$\sigma = \frac{1}{\sqrt{2} \times CPE_W} \quad (6)$$

where CPE_W is the value of constant phase element associated with the Warburg impedance. According to the results, Figure 13, it seems clear a diffusional behaviour. As it has been highlighted previously, the value of the exponent of the CPE used to simulate the diffusional behaviour at low frequencies is higher ($n \sim 0.7$) to that expected for a pure Warburg impedance ($n = 0.5$). Nevertheless, the time constant has to be related to a diffusive process. In order to estimate the σ values the CPE_W can be assimilated to a CPE_{dif} obtained from the simulation. The σ values are similar, of the order hundreds of $\Omega \cdot s^{-1/2}$ regardless of the sample and the immersion time.

Figure 15 shows the R_{ct}/σ values for the textured and un-textured aluminium 2024-T3 samples evaluated along the immersion time. R_{ct} can be deduced from the simulation. In all cases, the R_{ct}/σ ratio describes values higher than 1 but lower than 10 regardless of immersion time, which indicates that the corrosion mechanism for all samples is under a mixed control. This would not be in contradiction with the aforementioned on polarization curves, but would also strengthen it.

The results of electrochemical impedance spectroscopy revealed that the generation of texture patterns on aluminum alloy 2024-T3 by picoseconds laser texturing does not modify the corrosion mechanism, which is under a mixed control.

Nevertheless, and despite the extremely high peak temperatures (at least the material boiling point, 2743 K (2470 °C), which is the minimum temperature needed to evaporate the alloy) reached during each laser pulse, it seems there is no measurable heat diffusion that could lead to changes in alloy microstructure and initiate negative corrosion effects. Therefore, the laser texturing could be a promising treatment for other aluminium alloys to obtain new

functionalities with no detrimental effect in its corrosion behaviour. This aspect is very important, because it shows that the process does not limit the initial properties of the alloy in relation to its resistance to corrosion. Hence, the laser textures (and the ps laser process used to create them) allow the treated alloy to be used under the same conditions as those of an un-textured material, but with the advantage of added surface functionality. Applying surface textures to aluminium alloys in this way may then yield potentially important improvements in adherence, tribology and other properties.

4. Conclusions

1. Suitable combinations of fluence, number of pulses and scanning speed from a ps-laser system allow surface textures with differing geometries and topographies to be created on AA 2024-T3 surfaces.
2. SEM analysis revealed that no re-dissolution of the present phases occurred at the surface after the laser treatment. Instead, the evaporation effect of ablation that creates the surface texture features takes place without modification of the microstructure.
3. The un-textured samples and the surface with 5-50 % dimples showed hydrophilic nature while the crossed grooves and the concentric rings exhibited a hydrophobic character presumably due to changes in roughness.
4. The polarization curves showed that the all systems present similar corrosion current density.
5. Electrochemical impedance spectroscopy diagrams show two time constants, the first one at medium frequencies related to a charge transfer resistance process and a second one at low frequency due to a diffusion process.
6. The electrochemical tests reveal no differences in corrosion behaviour of the textured samples in comparison with the un-textured AA2024 alloy.

5. Acknowledgement

This work was supported by the Spanish Ministry of Science and Innovation [SMOTI MAT2009-13751] and the Spanish Ministry of Economy and Competitiveness [MAT2013-48224-C2-1-R-MUNSUTI].

6. References

- [1] W.M. Steen, J. Mazumder, *Laser Material Processing* (4th Edition), Springer-Verlag, London, 2010, pp. 295-347.
- [2] T. Ibatan, M.S. Uddin, M.A.K. Chowdhury, Recent development on surface texturing in enhancing tribological performance of bearing sliders. *Surface and Coatings Technology* 272 (2015) 102-120.
- [3] R. Kromer, S. Costil, J. Cormier, D. Courapied, L. Berthe, P. Peyre, M. Boustie, Laser surface patterning to enhance adhesion of plasma sprayed coatings. *Surface and Coatings Technology* 278 (2015) 171-182.
- [4] T. Dursun, C. Soutis, Recent developments in advanced aircraft aluminium alloys. *Mater. Des.* 56 (2014) 862-871
- [5] Z. Liu, C. Guzmán, H. Liu, A. Anacleto, T. Francisco, M. Abdoalshafie, L. Ma, O. Abodunrin, P. Skeldon, Corrosion performance and restoration of laser-formed metallic alloy sheets, *Journal of Laser Applications* 21 (2009), 76-81.
- [6] F. Viejo, A.E. Coy, F.J. Garcia-Garcia, Z. Liu, P. Skeldon, G.E. Thompson, Relationship between microstructure and corrosion performance of AA2050-T8 aluminium alloy after excimer laser surface melting, *Corros. Sci.* 52 (2010) 2179–2187.
- [7] W. L. Xu, T. M. Yue, H. C. Man, Nd:YAG laser surface melting of aluminium alloy 6013 for improving pitting corrosion fatigue resistance. *J Mater Sci* (2008) 43:942–951
- [8] U. Trdan, S. Žagar, J. Grum, J. L. Ocaña, Surface modification of laser- and shot-peened 6082 aluminium alloy: Laser peening effect to pitting corrosion. *International Journal of Structural Integrity*, 2 (2011) 9-21.
- [9] M.M. Quazi, M.A. Fazal, A.S.M.A. Haseeb, F. Yusof, H.H. Masjuki, A. Arslan, Laser-Based Surface Modifications of Aluminum and Its Alloys. *Crit. Rev. Solid State Mater. Sci.*, 41 (2016) 106-131.
- [10] A.S. Toloei, V. Stoilov, D.O. Northwood, A new approach to combating corrosion of metallic materials, *Applied Surface Science* 284 (2013) 242– 247.

- [11] Y. Jin, O.J. Allegre, W. Perrie, K. Abrams, J. Ouyang, E. Fearon, S.P. Edwardson, G. Dearden, Dynamic modulation of spatially structured polarization fields for real-time control of ultrafast laser-material interactions, *Optics Express* 21 (2013), 25333-25343.
- [12] R.P. Wei, C.M. Liao, M. Gao, A transmission electron microscopy study of constituent-particle-induced corrosion in 7075-T6 and 2024-T3 aluminum alloys. *Metall. Trans. A*, 29 (1998) 1153-1160.
- [13] A. E. Hughes, C. MacRae, N. Wilson, A. Torpy, T. H. Muster and A. M. Glenn, "Sheet AA2024-T3: a new investigation of microstructure and composition". *Surf. Interface Anal.* 42 (2010) 334–338
- [14] R. G. Buchheit, R. P. Grant, P. F. Hlava, B. Mckenzie, and G. L. Zender, "Local Dissolution Phenomena Associated with S Phase (Al₂CuMg) Particles in Aluminum Alloy 2024-T3. *J. Electrochem. Soc.*, 144 (1997) 2621-2628.
- [15] Y. Jin, W. Perrie, P. Harris, O.J. Allegre, K.J. Abrams, G. Dearden, Patterning of Aluminium thin film on polyethylene terephthalate by multi-beam picosecond laser, *Optics and Lasers in Engineering*, 74 (2015) 67-74.
- [16] I. Vlădoiu, M. Stafe, C. Neagu, I.M. Popescu, Nanopulsed ablation rate of metals dependence on the laser fluence and wavelength in atmospheric air. *U.P.B. Sci. Bull., Series A*, 70 (2008) 119-126.
- [17] D.Kam, S. Bhattacharya, J. Mazumder, Control of the wetting properties of an AISI 316L stainless steel surface by femtosecond laser-induced surface modification. *Journal of Micromech. Microeng.*, 22 (2012) p. 105019 (6 pp).
- [18] G. McHale, N. J. Shirtcliffe and M. I. Newton, "Super-hydrophobic and super-wetting surfaces: Analytical potential?" *Analyst*, 129 (2004) 284-287.
- [19] T. Koishi, K. Yasuoka, S. Fujikawa, T. Ebisuzaki, and X. C. Zeng, "Coexistence and transition between Cassie and Wenzel state on pillared hydrophobic surface". *Proceedings of the National Academy of Sciences U.S.A.* 106 (2009) 8435-8440.
- [20] A.M. Kietzig, S.G. Hatzikiriakos, and P.Englezos, "Patterned Superhydrophobic Metallic Surfaces". *Langmuir*, 25 (2009) 4821-4827.

- [21] V.D. Ta, A. Dunn, T. J. Wasley, J. Li, R. W. Kay, J. Stringer, P. J. Smith, E. Esenturk, C. Connaughton, J. D. Shephard, "Laser textured surface gradients". *Applied Surface Science* 371 (2016) 583–589.
- [22] J.A. DeRose, A. Bałkowiec, J. Michalski, T. Suter, K.J. Kurzydłowski, P. Schmutz, Aluminium alloy corrosion of aircraft structures, *WIT Transactions on State of the Art in Science and Engineering*, 61 (2012) 23-28.
- [23] J. Li, N. Birbilis, R. G. Buchheit, Electrochemical assessment of interfacial characteristics of intermetallic phases present in aluminium alloy 2024-T3. *Corros. Sci.*, 101 (2015) 155-164.
- [24] A.E. Hughes, R. Parvizi, M. Forsyth, Microstructure and corrosion of AA2024. *Corros. Rev.*, 33 (2015)1-30.
- [25] Y.L. Cheng, Z. Zhang, F.H. Cao, J.F. Li, J.Q. Zhang, J.M. Wang, C.N. Cao, A study of the corrosion of aluminum alloy 2024-T3 under thin electrolyte layers. *Corros. Sci.*, 46 (2004) 1649-1667.
- [26] E. McCafferty, *Introduction to Corrosion Science*. Chapter 8 "Concentration Polarization and Diffusion" pp.177-208. Springer Science+Business Media, LLC 2010.
- [27] A. E. Hughes, N. Birbilis, J.M.C. Mol, S. J. Garcia, X. Zhou and G. E. Thompson, Recent Trends in Processing and Degradation of Aluminium Alloys, *InTech*, 2011, pp.223-262. Available from: <http://www.intechopen.com/books/recent-trends-in-processing-and-degradation-of-aluminium-alloys/high-strength-al-alloys-microstructure-corrosion-and-principles-of-protection>. DOI: 10.5772/18766
- [27] M. Kendig , Simplified Analysis of EIS for Conversion Coated Aluminum Undergoing Pitting. *ECS Transactions*, 3 (2007) 153-163.
- [28] A. J. Bard, L. R. Faulkner, "Electrochemical methods. Fundamentals and Applications". John Wiley & Sons, Inc., New York, 2001, pp.368-416.